optica

# Doubly resonant second-harmonic generation of a vortex beam from a bound state in the continuum

Jun Wang,[1,*] Marco Clementi,[2] Momchil Minkov,[3] Andrea Barone,[2] Jean-François Carlin,[1] Nicolas Grandjean,[1] Dario Gerace,[2] Shanhui Fan,[3] Matteo Galli,[2] and Romuald Houdré[1]

[1]Institute of Physics, École Polytechnique Fédérale de Lausanne (EPFL), Switzerland
[2]Dipartimento di Fisica, Università di Pavia, Italy
[3]Department of Electrical Engineering, Stanford University, Stanford, California 94305, USA
*Corresponding author: jun.wang@epfl.ch

Received 28 April 2020; revised 20 July 2020; accepted 26 July 2020 (Doc. ID 396408); published 3 September 2020

**Second-harmonic generation in nonlinear materials can be greatly enhanced by realizing doubly resonant cavities with high quality factors. However, fulfilling such doubly resonant condition in photonic crystal (PhC) slab cavities is a long-standing challenge, because of the difficulty in engineering photonic bandgaps around both frequencies. Here, by implementing a second-harmonic bound state in the continuum (BIC) and confining it with a heterostructure design, we show the first doubly resonant PhC slab cavity with $2.4 \times 10^{-2}$ $W^{-1}$ intrinsic conversion efficiency under continuous-wave excitation. We also report the confirmation of highly normal-direction concentrated far-field emission pattern with radial polarization at the second harmonic frequency. These results represent a solid verification of previous theoretical predictions and a cornerstone achievement, not only for nonlinear frequency conversion but also for vortex beam generation and prospective nonclassical sources of radiation.** 

https://doi.org/10.1364/OPTICA.396408

## 1. INTRODUCTION

The interaction of electromagnetic radiation with an optical medium may lead to a multitude of nonlinear processes due to the intrinsic material susceptibilities, such as the $\chi^{(2)}$ tensor. The latter is responsible for, e.g., frequency upconversion (second-harmonic generation, SHG) and downconversion (spontaneous parametric downconversion, SPDC), among other frequency mixing processes. Enhancing such processes is desirable for many applications including nonlinear spectroscopy [1], frequency doubling of infrared laser sources to the visible or near-infrared, biosensing [2,3], quantum frequency conversion [4–6], and generation of nonclassical radiation [7–10].

In SHG and SPDC, in particular, the conversion efficiency can be strongly enhanced in doubly resonant cavities, i.e., simultaneously supporting resonant modes at either first- (FH) or second-harmonic (SH) frequencies, respectively [11–14]. In such cavities, nonlinear processes are enhanced by the quality (Q) factors of the two modes (i.e., increased temporal confinement), as well as by the spatial field confinement. The latter condition additionally requires that a large spatial overlap between the two fields is fulfilled, which generalizes the phase-matching condition in propagating geometries [15]. Doubly resonant conditions have been proposed and experimentally demonstrated in dual period Bragg mirrors [16–18], birefringently phase-matched waveguides [19], geometric dispersion-tuned microring resonators [20,21], and plasmonic nanoantennas [22]. Photonic crystal (PhC) defect cavities patterned in two-dimensional (2D) slabs, which allow for very tight field confinement in purely dielectric resonators, have been shown to produce significant SHG enhancement in a singly resonant regime at FH [23–31]. However, implementing a doubly resonant condition in PhC slab cavities is a longstanding challenge, because the SH frequency range generally lies entirely inside the light cone of the cladding materials, such that efficient confinement in the out-of-plane direction is prevented, not to mention the difficulty of engineering photonic bandgaps around both frequencies to favor the in-plane confinement.

Recently, a theoretical design based on a bound state in the continuum (BIC) opened up a new path for doubly resonant cavities on PhC slabs [32]. The BIC, in the case of a PhC slab, corresponds to the mode that lies inside the light cone but is nevertheless nonradiative, either because of symmetry protection or because of destructive interference between different radiation channels [33–35]. BICs have been theoretically proposed and experimentally implemented to enhance nonlinear generation in singly resonant regime [36–38]. The doubly resonant PhC cavity design [32] abandoned the commonly held notion of engineering photonic bandgaps at both FH and SH frequencies. Instead, at SH frequency, a BIC of PhC slab is engineered to provide the out-of-plane confinement, and a heterostructure of hexagonal lattice

is introduced to ensure the in-plane confinement in the absence of a photonic bandgap [39]. On the other hand, at FH frequency, the confinement mechanism is the same as in a conventional singly resonant PhC cavity, i.e., total internal reflection for the out-of-plane confinement and photonic bandgap for the in-plane confinement [29].

The BIC effect in the heterostructure cavity is highly interesting beyond simply being a means to achieve a long-lived mode at SH. In fact, BICs in PhC slabs are associated with a topological charge and are robust to structural modifications [35]. Strikingly, this topological charge manifests itself in the far-field radiation in the vicinity of a BIC in momentum space. Specifically, it was shown that the far-field must be linearly polarized and that, since the emission goes to zero at the BIC, the polarization angle must have a nontrivial winding around it [35]. This has also been demonstrated experimentally [40]. In Ref. [35], it was also proposed that this effect could be used to create vortex beam lasing [41], which can find applications in, e.g., optical trapping [42], light focusing and imaging [41,43], and communications [44].

Here we make use of such doubly resonant PhC cavity design and experimentally demonstrate highly efficient SHG in a small-footprint device fabricated in epitaxially grown highly nonlinear wide-bandgap GaN material. We also confirm that the SHG signal is a highly normal-direction concentrated vortex beam with radial polarization. This allows for an extremely high collection efficiency even with a small numerical aperture of the collecting lens, which is different from previous SHG realizations in singly resonant PhC cavities [24,25,27,29].

## 2. EXPERIMENT

### A. Cavity Design

The basic structure of the cavity is a 2D PhC made from a hexagonal lattice of air holes in a slab, where the lattice constant is $a$, the air hole radius is $r$, the slab thickness is $d$, and the refractive index is $n$ [32]. The PhC slab is suspended in air, and external light could be coupled to the cavity from the top side of the slab [Fig. 1(a)]. A heterostructure design is introduced to the PhC slab by increasing the hole radii $(r_c, r_t, r_o)$ in three concentric hexagonal regions (core, transition, and outer) whose sizes are defined by the side-lengths in units of lattice constant $(N_c, N_t, N_o)$ [Fig. 1(b)]. The heterostructure introduces a defect mode inside the photonic bandgap of the outer region at FH frequency, while at the same time provides a resonant mode at SH frequency in the absence of a photonic bandgap. The out-of-plane confinement is guaranteed by the total internal reflection of the slab at FH frequency, and by the quasi-BIC at SH frequency (see Supplement 1, Fig. S4). The Q-factor at FH increases with the sizes of both the core and the outer regions, while the Q-factor at SH increases mainly with the size of the core region from which the quasi-BIC is derived. Although a larger core region results in larger Q-factors at both frequencies, the nonlinear overlap factor decreases with reduced spatial confinement; thus, an optimized core size should be considered to favor a high conversion efficiency.

Far-field emission pattern at FH frequency is engineered with band-folding technique, which slightly increases the hole radii, with lattice period $2a$, by $\Delta r_c$ and $\Delta r_t$ in the core and transition regions, respectively. The holes with increased radii are referred to as injectors (or extractors), and their radii are $r_{c,\mathrm{inj}}$ and $r_{t,\mathrm{inj}}$, respectively. This technique folds the k-vector components at the

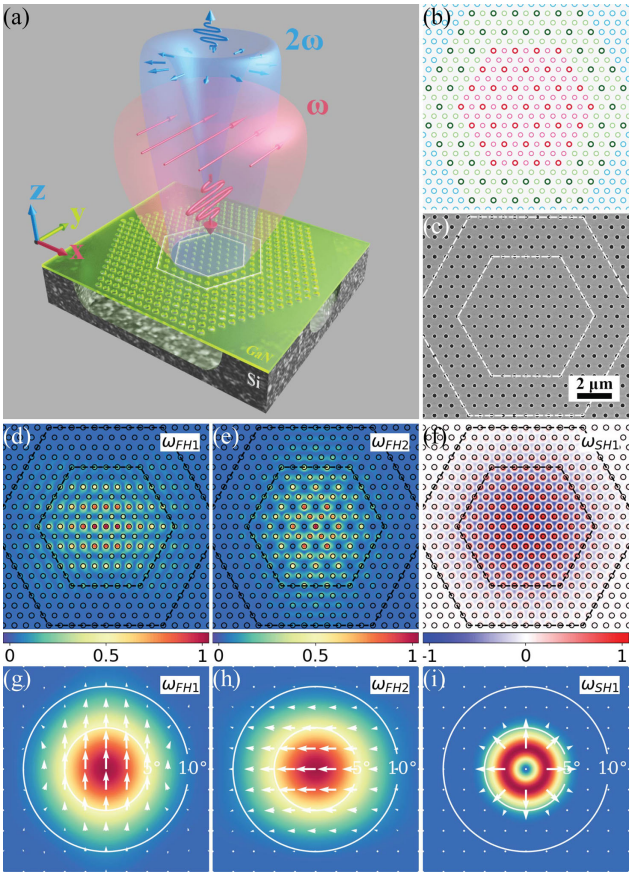


**Fig. 1.** (a) Conceptual rendering of the SHG in a doubly resonant PhC slab cavity under linearly polarized beam excitation. The red and the blue lobes represent the far-field intensities of the FH and SH modes, respectively, on the upper side of the slab. (b) Design of a doubly resonant cavity with parameters: $a = 650$ nm, $N_c = 6$, $N_t = 4$, $N_o = 14$, $r_c = 130$ nm, $r_t = 137$ nm, $r_o = 150$ nm, $r_{c,\mathrm{inj}} = 140$ nm, $r_{t,\mathrm{inj}} = 147$ nm. The core, transition, and outer regions are in red, green, and blue, respectively. The injectors in the core and transition regions are emphasized with crimson and dark green. (c) SEM image of the cavity. The core and transition regions are outlined by white dashed hexagons. (d)–(i) Near-field and far-field patterns of the designed cavity given by simulation (see Supplement 1 for high-order modes). (d) and (e) Intensity of the squared electric field, $|E_x^2 + E_y^2|$, at the center of the slab for the first two degenerate resonant modes at FH. (f) Electric field amplitude, $\mathrm{Re}(E_z)$, at the center of the slab for the first resonant mode at SH. (g)–(i) Far-field emission pattern for the first two degenerate resonant modes at FH and the first resonant mode at SH. The color map shows the intensity of the squared electric field, $|\boldsymbol{E}|^2$; the overlaid arrows show the field vectors, $[\mathrm{Re}(E_x), \mathrm{Re}(E_y)]$; the circles from inside out mark the emission angles of 5° and 10°.

Brillouin zone edge to the Γ-point in the reciprocal space, which concentrates the FH emission to the normal direction of the PhC slab and thus increases the in-coupling efficiency of the pumping beam [45,46], however at the expense of Q-factor at FH.

The resonant modes at FH and SH were designed at wavelengths around 1550 nm and 775 nm, respectively, for which the design parameters are $a = 650$ nm, $N_c = 6$, $N_t = 4$, $N_o = 14$, $r_c = 130$ nm, $r_t = 137$ nm, $r_o = 150$ nm, $r_{c,\mathrm{inj}} = 140$ nm, $r_{t,\mathrm{inj}} = 147$ nm, $d = 214$ nm [Fig. 1(b)]. Theoretical simulations have been performed by three-dimensional finite-difference time domain (3D-FDTD), in which the refractive indices used were $n = 2.28$ at FH and $n = 2.31$ at SH, respectively, to account for material dispersion. The simulated near-field

patterns of the first two degenerate FH modes and the first SH mode are shown in Figs. 1(d)–1(f), while the corresponding far-field patterns are shown in Figs. 1(g)–1(i). The FH mode is predominantly TE-polarized while the SH mode is predominantly TM-polarized (with respect to the slab plane), and the two are coupled through the $xxz$ and $yyz$ components of the GaN second-order susceptibility tensor.

Since the dependencies of FH and SH resonant frequencies on the PhC parameters, such as the lattice constant $a$, the hole radius $r$, and the slab thickness $d$, are different, lithographic tuning of these parameters will help to achieve the doubly resonant condition [32]. In practice, the lattice constant $a$, the hole radii $r$, and the slab thickness $d$ are scanned around the target values to verify the predicted dependencies, and also to compensate for fabrication imperfections and uncertainty of the refractive index in the experiment compared with the values used in the simulation.

## B. Fabrication

GaN was chosen to be the slab material because of the perfect combination of a large nonlinear susceptibility and a wide bandgap that accommodates the optical transmission for both pumping wavelengths at the telecom band and SHG wavelength at visible. The fabrication process is similar to that in previous works [29,47]. The GaN film (around 200 nm) was grown hetero-epitaxially on Si(111) substrate along the $c$ axis ($z$ direction) by metal-organic chemical vapor deposition (MOCVD) at typically 1000°C. The Si(111) substrate is placed such that one of the cleavage planes is along the $y$ direction. An aluminum nitride (AlN) buffer layer (around 40 nm) was grown prior to GaN with the same condition to mitigate the lattice mismatch.

The PhC was fabricated through a two-step ZEP-$SiO_2$ electron beam lithography. First, a layer of 100 nm $SiO_2$ was grown on the GaN surface by plasma enhanced chemical vapor deposition (PECVD). Then a layer of around 50 nm positive resist (ZEP520A) was spin-coated on top of $SiO_2$ and was patterned by electron beam (Vistec EBPG5000+). After development, the pattern in the resist was transferred to $SiO_2$ layer to form a hard mask by inductively coupled plasma reactive ion etching (ICP-RIE). After removal of ZEP residue (by remover-1165), another step of ICP-RIE dedicated to III-nitride was applied to transfer the pattern from $SiO_2$ hard mask to GaN/AlN layer. Finally, after removal of residual $SiO_2$ by hydrogen fluoride (HF), isotropic xenon difluoride ($XeF_2$) gas etching was applied to under-etch the Si substrate through holes in the GaN/AlN layer, and an air gap around 2 μm was created. A scanning electron microscope (SEM) image of the fabricated cavity is shown in Fig. 1(c).

## C. Characterization

### 1. Resonances and Detuning

A resonant scattering (RS) technique [48] was employed to characterize the cavity resonances at both FH and SH wavelengths. At FH range (around 1550 nm wavelength), the cavity was excited by a linearly polarized beam at normal incidence with E-field at 45° from the $x$ axis of the cavity, knowing from simulations [32] that the resonant modes are linearly polarized along the $x$ or $y$ axis [Figs. 1(g) and 1(h)]. Typically five peaks are visible within 5 nm range, and they are indexed as $FH_1$, $FH_2$, and so on from long wavelength to short [Fig. 2(a)]. A Q-factor of $2.0 \times 10^4$ can be measured for $FH_1$, which is comparable with those measured in

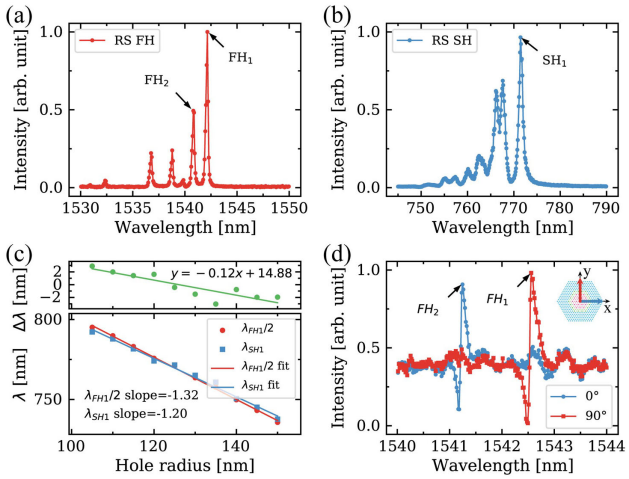


**Fig. 2.** (a) and (b) Typical resonant scattering (RS) spectra at FH and SH, obtained by supercontinuum broadband excitation and spectrometer detection. (c) Dependencies of the resonant wavelength (λ) and the detuning (Δλ) on the hole radius of the core region. The radius increments for the transition region and the outer region are the same as for the core region. (d) FH resonant scattering spectra for different incident polarizations, after removal of the analyzer. The first mode ($FH_1$) is excited by polarization at around 90° from $x$ axis while the second mode ($FH_2$) is excited by polarization at around 0°. The inset shows the configuration of the polarizer with respect to the cavity. The asymmetric (Fano) line shape observed is due to the coherent interference between the backreflected light and the signal emitted from the cavity.

GaN-based L3 and H0 singly resonant cavities [29]. The theoretical quality factor of the cavity without the extractors is $1.1 \times 10^5$, while the value with $\Delta r_c = 10$ nm is $2.6 \times 10^4$. This suggests that the measured quality factor is limited by the extractor size. Smaller extractors could thus lead to higher $Q$ and conversion efficiency since even the nominal cavity without extractors was found to have sizable far-field components in the vertical direction [32].

At SH range (around 775 nm wavelength), the mode was excited with the same configuration as for FH. The quasi-TM mode at SH could be excited because of nonzero overlap with the incident E-field. A sharp and intense peak can be observed, together with some higher-order peaks at smaller wavelengths [Fig. 2(b)]. Q-factor of around 800 can be measured while the theoretical value is around 2000. It should be noted that the high Q-factor observed at SH confirms the existence of a quasi-BIC mode since the PhC modes at this frequency lie entirely inside the line cone (see Supplement 1, Fig. S4). The Q-factor of the SH mode is mainly limited by the out-of-plane loss due to the limited size of the core region, while the in-plane leakage due to limited hole layers in the outer region of the cavity may also contribute. 3D-FDTD simulations suggest that the SH mode Q-factor is not sensitive to the extractor size.

An important characteristic of doubly resonant cavities is how the two resonances match simultaneously the FH and SH wavelengths. The detuning of the two resonances can be defined as

$$\Delta\lambda = \lambda_{FH}/2 - \lambda_{SH}, \tag{1}$$

where $\lambda_{FH}$ and $\lambda_{SH}$ are the resonant wavelengths at FH and SH, respectively. The intrinsic SHG conversion efficiency is defined as $P_g/P_c^2$, where $P_g$ is the SHG power from the cavity and $P_c$ is the coupled power to the cavity. By this definition, the intrinsic SHG

conversion efficiency is not dependent on the coupling efficiency nor on the extraction efficiency, and it follows [16]:

$$\eta_{\mathrm{conv}}(\lambda) \propto Q_{\mathrm{FH}}^2 Q_{\mathrm{SH}} \mathcal{L}_{\mathrm{FH}}^2(\lambda) \mathcal{L}_{\mathrm{SH}}(\lambda/2), \tag{2}$$

where $\lambda$ is the excitation wavelength, $Q_{\mathrm{FH}}$ and $Q_{\mathrm{SH}}$ are the Q-factors of FH and SH resonances respectively, $\mathcal{L}_{\mathrm{FH}}(\lambda)$ and $\mathcal{L}_{\mathrm{SH}}(\lambda)$ are the normalized intensities as a function of wavelength for FH and SH resonances, respectively, and they take the form of Lorentzian function $1/(1+(\lambda-\lambda_0)^2/(\Gamma/2)^2)$, where $\lambda_0$ is the resonant wavelength and $\Gamma = \lambda_0/Q$. When exciting the cavity at FH resonance, i.e., $\lambda = \lambda_{\mathrm{FH}}$, the detuning $\Delta\lambda$ determines the intrinsic conversion efficiency $\eta_{\mathrm{conv}}$ via $\mathcal{L}_{\mathrm{SH}}(\lambda_{\mathrm{FH}}/2)$, and the smaller the detuning, the higher the conversion efficiency.

As mentioned before, the PhC parameters, such as lattice constant $a$, hole radius $r$, and slab thickness $d$, are lithographically scanned to match the doubly resonant condition. The dependencies of $\lambda_{\mathrm{FH}}$ on PhC hole radius $r$ is observed to be more sensitive than that of $\lambda_{\mathrm{SH}}$; thus, a crossing with the zero level shows up for detuning as a function of hole radius at around the target wavelength, which is in agreement with theoretical predictions [32] [Fig. 2(c)]. Similar crossings for detuning as a function of lattice constant and slab thickness are also observed (see Supplement 1).

### 2. FH Cavity Mode Polarization

The polarization of the first two FH modes was investigated by exciting the cavity with incident beams at different polarization angles. The experimental setup was modified from the RS one [48] by introducing a $\lambda/2$ wave plate after the polarizer and removing the analyzer. Wavelength scans were performed around the FH modes with different polarization angles. The results show that the mode $FH_1$ is excited at around 90° (from the $x$ axis of the cavity) polarization while the mode $FH_2$ at around 0° [Fig. 2(d)].

It should be noted that, from a theoretical standpoint, the sixfold rotational symmetry of the structure and the double degeneracy of the lowest energy (fundamental) mode allow us to identify different pairs of modes for $FH_1$ and $FH_2$, which can be expressed as linear combinations of the modes represented in Figs. 1(g) and 1(h) [49]. On the other hand, the degeneracy is here resolved by the presence of fabrication disorder; as a result, the presence of disorder ultimately fixes the polarization of the $FH_1$ and $FH_2$ modes. Nevertheless, it can be noticed that (1) the orthogonality of the modes polarization is respected despite the splitting, consistently with theory [49], and (2) the preferable direction for the modes polarization is still along the $x$ and $y$ axes, probably due to their peculiar role as crystallographic axes and/or due to the privileged frame of reference introduced by electron beam lithography.

In conclusion, the $FH_1$ and $FH_2$ mode polarization is always orthogonal and lies mainly along the crystallographic axes [traces 0° and 90° in Fig. 2(d)]. A slight deviation from this condition is observed on some devices, owing to the random effect of disorder [see Fig. 3(d) in the next section].

### 3. Second-Harmonic Generation

The SHG was investigated by exciting the cavity with a linearly polarized laser beam, at normal incidence. The orientation of the electric field for the pump beam was arbitrarily varied by means of a $\lambda/2$ waveplate. The collimated beam from a tunable continuous-wave laser source was focused on the cavity by a microscope objective (20×, NA = 0.4), and the coupling to cavity was optimized by fine translation of the sample in $x$, $y$, and $z$ directions using a piezoelectric stage. The SHG signal was collected through the same objective, redirected by a dichroic mirror, and detected with a Si photodetector in free space.

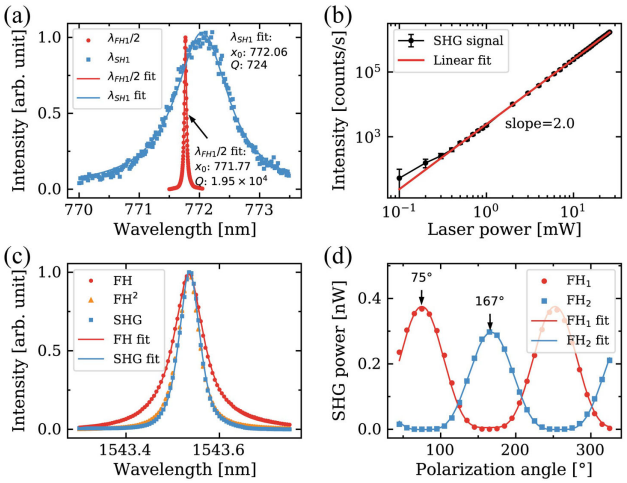


**Fig. 3.** (a) Normalized resonant scattering intensity at FH and SH as a function of excitation wavelength, for a cavity with −0.3 nm detuning. Continuous lines show Lorentzian fits. (b) SHG intensity as a function of excitation power at resonance. (c) Normalized resonant scattering intensity at FH and SHG intensity as a function of excitation wavelength. Continuous lines show Lorentzian and Lorentzian-squared fits for FH and SHG data, respectively. (d) SHG signal at $FH_1$ and $FH_2$ as a function of incident polarization angle. Continuous lines show $\cos^4$ fits.

**Table 1. Comparison of SHG in Two Cavities[a]**

| | $\Delta\lambda$ (nm) | $Q_{\mathrm{FH}}$ ($\times 10^4$) | $Q_{\mathrm{SH}}$ | $\mathcal{L}_{\mathrm{SH}}(\lambda_{\mathrm{FH}}/2)$ | $\eta_c$ (%) | $P_c$ (mW) | $P_g$ (nW) | $\eta_{\mathrm{conv}}$ ($\mathrm{W}^{-1}$) |
|---|---|---|---|---|---|---|---|---|
| 1 | −0.9 | 1.49 | 804 | 0.23 | 19.6 | 0.541 | 1.120 | $3.8 \times 10^{-3}$ |
| 2 | −0.3 | 1.95 | 724 | 0.77 | 6.9 | 0.125 | 0.372 | $2.4 \times 10^{-2}$ |

[a]$\Delta\lambda$ is the detuning, $Q_{\mathrm{FH}}$ and $Q_{\mathrm{SH}}$ are Q-factors for FH and SH resonances, $\mathcal{L}_{\mathrm{SH}}(\lambda_{\mathrm{FH}}/2)$ is the normalized SH intensity at FH resonance, $\eta_c$ is the coupling efficiency, $P_c$ is the coupled power, $P_g$ is the SHG power, and $\eta_{\mathrm{conv}}$ is the intrinsic conversion efficiency.

Two cavities are shown as examples (Table 1): one with large detuning (−0.9 nm) and the other with small detuning (−0.3 nm) [Fig. 3(a)]. The ratio of the two conversion efficiencies is very close to the value predicted by Eq. (2). Moreover, the record intrinsic conversion efficiency in the cavity with small detuning, $2.4 \times 10^{-2}\ \mathrm{W}^{-1}$ (±15%, assuming 100% collection efficiency on the upper side of the slab; see Supplement 1 for the calibration details), is 10 times larger than that of singly resonant L3 and H0 cavities [29] ($\eta_{\mathrm{conv}} = 2.4 \times 10^{-3}\ \mathrm{W}^{-1}$, $Q = 3.3 \times 10^4$), even with smaller Q-factor at FH, which confirms the great potential of this doubly resonant PhC cavity scheme for efficient nonlinear frequency conversion.

The SHG process is ascertained by power-dependent measurement: by fixing the excitation wavelength at $FH_1$, the SHG intensity scaled quadratically with the excitation power [Fig. 3(b)]. Alternatively, by fixing the excitation power and scanning the pumping wavelength, the SHG intensity exhibited Lorentzian-squared dependence and matched perfectly with the square of FH RS intensity, which also confirmed the quadratic nature of the SHG process [Fig. 3(c)].

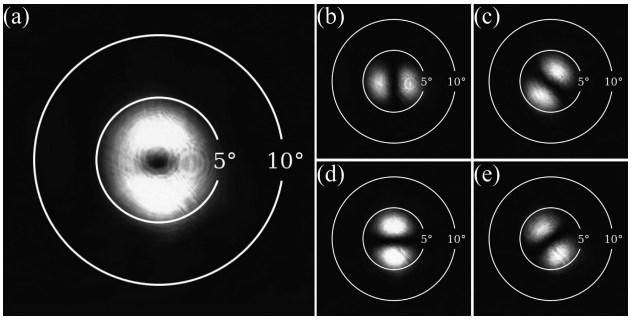


**Fig. 4.** (a) Fourier imaging of SH far-field emission pattern. The gray scale represents the captured intensity as a function of far-field emission angle. (b)–(e) Fourier imaging of SH far-field emission pattern with polarizer at 0°, 45°, 90°, and 135°, respectively.

Fine polarization scan shows that the SHG intensity is proportional to $\cos^4(\theta_p)$, where $\theta_p$ is the incident polarization angle, and the curve for $FH_2$ is dephased from $FH_1$ by about 90° [Fig. 3(d)]. Together with the previous RS experiment, this confirms that the polarization of mode $FH_1$ is around 90° (along with the $y$ axis of the cavity) while the polarization of mode $FH_2$ is around 0° (along with the $x$ axis of the cavity). The 180° period of both modes and the $\cos^4$ dependence are consistent with the assumption of linear polarization of cavity modes at FH.

#### 4. SH Far-Field Emission Pattern

Theoretical analysis and 3D-FDTD simulation predict that the far-field emission at SH frequency is a linearly polarized vortex beam with a donut-shaped intensity pattern and radial polarization [Fig. 1(i)]. This is consistent with the topological nature of BICs in momentum space [35]. To verify this, the SHG far-field emission pattern was investigated by Fourier imaging. After passing through the microscope objective and being redirected by a dichroic mirror, the SHG beam was focused by a lens to form an image of the back focal plane of the objective on a CCD array, and a donut-shaped pattern was directly captured [Fig. 4(a)]. The donut-shaped far-field pattern is concentrated within a ±5° angle in air, which is in perfect agreement with the simulation.

Moreover, when placing a polarizer film in front of the CCD array, a pattern of two lobes always remains, and its axis, which crosses the centers of the lobes, is always aligned with the polarizer, which confirms the radially polarized nature of the beam [Figs. 4(b)–4(e)].

## 3. DISCUSSION

The 3D-FDTD simulation predicts two degenerate modes at FH wavelength with linear polarization of the far-field emission along the $x$ axis and $y$ axis, respectively [32], while the RS experiment and the fine polarization rotation in SHG experiment show two separated peaks with orthogonal polarization. This suggests that the two orthogonal modes are split in wavelength because of symmetry breaking, commonly observed in optical microcavities affected by disorder [50]. Further 3D-FDTD simulations show that material birefringence and geometrical symmetry breaking (e.g., elliptical holes) can split the degeneracy of the FH mode.

The BIC resonant mode at SH produces a linearly polarized vortex beam with radially winding polarization, which confirms the topological charge description [35]. Although the BIC resonant mode is not the only way of generating a radially polarized beam [51], the highly normal-direction concentration of beam in this work is peculiar and takes advantage in beam outcoupling. Simulations suggest that the symmetry of the far-field emission pattern could be broken by material birefringence and geometry deformation. In practice, the small anisotropy with a higher intensity of the far-field emission pattern in $y$ direction suggests systematic symmetry breaking both at material and geometrical levels, which is consistent with the split peaks at FH.

Although the optimization of material quality and Q-factors were not the main targets during the fabrication process, the Q-factors are comparable with the predicted values, and the SHG conversion efficiencies are significantly higher than those in singly resonant cavities made of comparable materials and through similar fabrication processes. This shows the robustness of the present design and suggests great potential for improvement in the Q-factors and conversion efficiency. Alternative doubly resonant cavity designs have been proposed, based on topology optimization of microposts and microrings [15,52]. However, these designs contain very fine structural features that make them less robust to fabrication imperfections in practice. Further design based on cylindrical dielectric structures has also been demonstrated [53], characterized by a high degree of compactness and sustaining quite high excitation powers. However, the measured Q-factors and conversion efficiencies are much lower than the ones shown in the present work, and the BIC mode is in an FH range that requires a vortex beam for efficient pumping, which is less convenient than pumping with linearly polarized beams as in the present case.

## 4. CONCLUSION

We have experimentally demonstrated the first doubly resonant PhC slab cavity, whose Q-factors at FH (around 1550 nm) and SH (around 775 nm) are around $2.0 \times 10^4$ and 800, respectively. An experimental intrinsic SHG conversion efficiency of $2.4 \times 10^{-2}\ \mathrm{W}^{-1}$ is achieved, which is 10 times larger than the previously shown result for a singly resonant cavity with similar material (i.e., GaN by MOCVD on Si) and processing technique. We also confirmed that the SHG emission pattern is tightly concentrated (±5°) around the normal direction with donut shape and radial polarization, which originate from the BIC mode at SH.

In this work, the implementation of the BIC and the heterostructure put forward a practical realization to the long-standing challenge of designing PhC slab cavities fulfilling the doubly resonant conditions. We notice that significant room for improvement is left for further developments, both at the level of nonlinear overlap factor design and experimental Q-factors, and thus the SHG conversion efficiency could be ultimately increased in the future. Specific features such as tight light confinement, controllable wavelength detuning, and highly normal-direction concentration of both FH and SH emissions make this design an ideal platform for on-chip nonlinear light manipulation. In addition, the BIC confinement mechanism provides a natural way to generate a highly concentrated and radially polarized vortex beam through the SHG process.

**Funding.** Schweizerischer Nationalfonds zur Förderung der Wissenschaftlichen Forschung (2000020-169560, 200020-188649); Università degli Studi di Pavia (Dipartimenti di

Eccellenza Program (2018-2022), Horizon 2020 Framework Programme (H2020), project CUSPIDOR, QuantERA ERA-NET); Air Force Office of Scientific Research (FA9550-17-1-0002).

**Disclosures.** The authors declare no conflicts of interest.

See Supplement 1 for supporting content.

## REFERENCES


1. T. F. Heinz, C. K. Chen, D. Ricard, and Y. R. Shen, "Spectroscopy of molecular monolayers by resonant second-harmonic generation," Phys. Rev. Lett. **48**, 478–481 (1982).
2. P. J. Campagnola and L. M. Loew, "Second-harmonic imaging microscopy for visualizing biomolecular arrays in cells, tissues and organisms," Nat. Biotechnol. **21**, 1356–1360 (2003).
3. E. Estephan, D. Bajoni, M.-B. Saab, T. Cloitre, R. Aulombard, C. Larroque, L. C. Andreani, M. Liscidini, A. M. Malvezzi, and C. Gergely, "Sensing by means of nonlinear optics with functionalized GaAs/AlGaAs photonic crystals," Langmuir **26**, 10373–10379 (2010).
4. S. Tanzilli, W. Tittel, M. Halder, O. Alibart, P. Baldi, N. Gisin, and H. Zbinden, "A photonic quantum information interface," Nature **437**, 116–120 (2005).
5. M. T. Rakher, L. Ma, O. Slattery, X. Tang, and K. Srinivasan, "Quantum transduction of telecommunications-band single photons from a quantum dot by frequency upconversion," Nat. Photonics **4**, 786–791 (2010).
6. S. Zaske, A. Lenhard, C. A. Keßler, J. Kettler, C. Hepp, C. Arend, R. Albrecht, W.-M. Schulz, M. Jetter, P. Michler, and C. Becher, "Visible-to-telecom quantum frequency conversion of light from a single quantum emitter," Phys. Rev. Lett. **109**, 147404 (2012).
7. A. Majumdar and D. Gerace, "Single-photon blockade in doubly resonant nanocavities with second-order nonlinearity," Phys. Rev. B **87**, 235319 (2013).
8. D. Gerace and V. Savona, "Unconventional photon blockade in doubly resonant microcavities with second-order nonlinearity," Phys. Rev. A **89**, 031803 (2014).
9. L. Caspani, C. Xiong, B. J. Eggleton, D. Bajoni, M. Liscidini, M. Galli, R. Morandotti, and D. J. Moss, "Integrated sources of photon quantum states based on nonlinear optics," Light Sci. Appl. **6**, e17100 (2017).
10. G. Marino, A. S. Solntsev, L. Xu, V. F. Gili, L. Carletti, A. N. Poddubny, M. Rahmani, D. A. Smirnova, H. Chen, A. Lemaître, G. Zhang, A. V. Zayats, C. D. Angelis, G. Leo, A. A. Sukhorukov, and D. N. Neshev, "Spontaneous photon-pair generation from a dielectric nanoantenna," Optica **6**, 1416–1422 (2019).
11. P. Drummond, K. McNeil, and D. Walls, "Non-equilibrium transitions in sub/second harmonic generation," Opt. Acta **27**, 321–335 (1980).
12. R. Paschotta, K. Fiedler, P. Kürz, and J. Mlynek, "Nonlinear mode coupling in doubly resonant frequency doublers," Appl. Phys. B **58**, 117–122 (1994).
13. V. Berger, "Second-harmonic generation in monolithic cavities," J. Opt. Soc. Am. B **14**, 1351–1360 (1997).
14. A. Rodriguez, M. Soljačić, J. D. Joannopoulos, and S. G. Johnson, "$\chi^{(2)}$ and $\chi^{(3)}$ harmonic generation at a critical power in inhomogeneous doubly resonant cavities," Opt. Express **15**, 7303–7318 (2007).
15. Z. Lin, X. Liang, M. Lončar, S. G. Johnson, and A. W. Rodriguez, "Cavity-enhanced second-harmonic generation via nonlinear-overlap optimization," Optica **3**, 233–238 (2016).
16. M. Liscidini and L. C. Andreani, "Second-harmonic generation in doubly resonant microcavities with periodic dielectric mirrors," Phys. Rev. E **73**, 016613 (2006).
17. K. Rivoire, S. Buckley, and J. Vučković, "Multiply resonant photonic crystal nanocavities for nonlinear frequency conversion," Opt. Express **19**, 22198–22207 (2011).
18. S. Buckley, M. Radulaski, J. L. Zhang, J. Petykiewicz, K. Biermann, and J. Vučković, "Multimode nanobeam cavities for nonlinear optics: high quality resonances separated by an octave," Opt. Express **22**, 26498–26509 (2014).
19. L. Scaccabarozzi, M. M. Fejer, Y. Huo, S. Fan, X. Yu, and J. S. Harris, "Enhanced second-harmonic generation in AlGaAs/AlxOy tightly confining waveguides and resonant cavities," Opt. Lett. **31**, 3626–3628 (2006).
20. W. H. P. Pernice, C. Xiong, C. Schuck, and H. X. Tang, "Second harmonic generation in phase matched aluminum nitride waveguides and microring resonators," Appl. Phys. Lett. **100**, 223501 (2012).
21. A. W. Bruch, X. Liu, X. Guo, J. B. Surya, Z. Gong, L. Zhang, J. Wang, J. Yan, and H. X. Tang, "17 000%/W second-harmonic conversion efficiency in single-crystalline aluminum nitride microresonators," Appl. Phys. Lett. **113**, 131102 (2018).
22. M. Celebrano, X. Wu, M. Baselli, S. Großmann, P. Biagioni, A. Locatelli, C. De Angelis, G. Cerullo, R. Osellame, B. Hecht, L. Duò, F. Ciccacci, and M. Finazzi, "Mode matching in multiresonant plasmonic nanoantennas for enhanced second harmonic generation," Nat. Nanotechnol. **10**, 412–417 (2015).
23. M. W. McCutcheon, J. F. Young, G. W. Rieger, D. Dalacu, S. Frédérick, P. J. Poole, and R. L. Williams, "Experimental demonstration of second-order processes in photonic crystal microcavities at submilliwatt excitation powers," Phys. Rev. B **76**, 245104 (2007).
24. K. Rivoire, Z. Lin, F. Hatami, W. T. Masselink, and J. Vučković, "Second harmonic generation in gallium phosphide photonic crystal nanocavities with ultralow continuous wave pump power," Opt. Express **17**, 22609–22615 (2009).
25. M. Galli, D. Gerace, K. Welna, T. F. Krauss, L. O'Faolain, G. Guizzetti, and L. C. Andreani, "Low-power continuous-wave generation of visible harmonics in silicon photonic crystal nanocavities," Opt. Express **18**, 26613–26624 (2010).
26. S. Yamada, B.-S. Song, S. Jeon, J. Upham, Y. Tanaka, T. Asano, and S. Noda, "Second-harmonic generation in a silicon-carbide-based photonic crystal nanocavity," Opt. Lett. **39**, 1768–1771 (2014).
27. S. Buckley, M. Radulaski, J. Petykiewicz, K. G. Lagoudakis, J.-H. Kang, M. Brongersma, K. Biermann, and J. Vučković, "Second-harmonic generation in GaAs photonic crystal cavities in (111)B and (001) crystal orientations," ACS Photon. **1**, 516–523 (2014).
28. Y. Zeng, I. Roland, X. Checoury, Z. Han, M. El Kurdi, S. Sauvage, B. Gayral, C. Brimont, T. Guillet, M. Mexis, F. Semond, and P. Boucaud, "Resonant second harmonic generation in a gallium nitride two-dimensional photonic crystal on silicon," Appl. Phys. Lett. **106**, 081105 (2015).
29. M. S. Mohamed, A. Simbula, J.-F. Carlin, M. Minkov, D. Gerace, V. Savona, N. Grandjean, M. Galli, and R. Houdré, "Efficient continuous-wave nonlinear frequency conversion in high-Q gallium nitride photonic crystal cavities on silicon," APL Photon. **2**, 031301 (2017).
30. B.-S. Song, T. Asano, S. Jeon, H. Kim, C. Chen, D. D. Kang, and S. Noda, "Ultrahigh-Q photonic crystal nanocavities based on 4H silicon carbide," Optica **6**, 991–995 (2019).
31. M. Clementi, K. Debnath, M. Sotto, A. Barone, A. Z. Khokhar, T. D. Bucio, S. Saito, F. Y. Gardes, D. Bajoni, and M. Galli, "Cavity-enhanced harmonic generation in silicon rich nitride photonic crystal microresonators," Appl. Phys. Lett. **114**, 131103 (2019).
32. M. Minkov, D. Gerace, and S. Fan, "Doubly resonant $\chi^{(2)}$ nonlinear photonic crystal cavity based on a bound state in the continuum," Optica **6**, 1039–1045 (2019).
33. C. W. Hsu, B. Zhen, A. D. Stone, J. D. Joannopoulos, and M. Soljačić, "Bound states in the continuum," Nat. Rev. Mater. **1**, 16048 (2016).
34. C. W. Hsu, B. Zhen, J. Lee, S.-L. Chua, S. G. Johnson, J. D. Joannopoulos, and M. Soljačić, "Observation of trapped light within the radiation continuum," Nature **499**, 188–191 (2013).
35. B. Zhen, C. W. Hsu, L. Lu, A. D. Stone, and M. Soljačić, "Topological nature of optical bound states in the continuum," Phys. Rev. Lett. **113**, 257401 (2014).
36. L. Carletti, K. Koshelev, C. De Angelis, and Y. Kivshar, "Giant nonlinear response at the nanoscale driven by bound states in the continuum," Phys. Rev. Lett. **121**, 033903 (2018).
37. L. Carletti, S. S. Kruk, A. A. Bogdanov, C. De Angelis, and Y. Kivshar, "High-harmonic generation at the nanoscale boosted by bound states in the continuum," Phys. Rev. Res. **1**, 023016 (2019).
38. L. Xu, K. Zangeneh Kamali, L. Huang, M. Rahmani, A. Smirnov, R. Camacho-Morales, Y. Ma, G. Zhang, M. Woolley, D. Neshev, and A. E. Miroshnichenko, "Dynamic nonlinear image tuning through magnetic dipole quasi-BIC ultrathin resonators," Adv. Sci. **6**, 1802119 (2019).

39. X. Ge, M. Minkov, S. Fan, X. Li, and W. Zhou, "Low index contrast heterostructure photonic crystal cavities with high quality factors and vertical radiation coupling," Appl. Phys. Lett. **112**, 141105 (2018).
40. H. M. Doeleman, F. Monticone, W. Den Hollander, A. Alù, and A. F. Koenderink, "Experimental observation of a polarization vortex at an optical bound state in the continuum," Nat. Photonics **12**, 397–401 (2018).
41. Q. Zhan, "Cylindrical vector beams: from mathematical concepts to applications," Adv. Opt. Photon. **1**, 1–57 (2009).
42. J. Ng, Z. Lin, and C. T. Chan, "Theory of optical trapping by an optical vortex beam," Phys. Rev. Lett. **104**, 103601 (2010).
43. K. Kitamura, K. Sakai, N. Takayama, M. Nishimoto, and S. Noda, "Focusing properties of vector vortex beams emitted by photonic-crystal lasers," Opt. Lett. **37**, 2421–2423 (2012).
44. J. Wang, "Advances in communications using optical vortices," Photon. Res. **4**, B14–B28 (2016).
45. S. Combrié, A. De Rossi, and N.-V.-Q. Tran, "Directive emission from high-*Q* photonic crystal cavities through band folding," Phys. Rev. B **79**, 041101 (2009).
46. S. L. Portalupi, M. Galli, C. Reardon, T. Krauss, L. O'Faolain, L. C. Andreani, and D. Gerace, "Planar photonic crystal cavities with far-field optimization for high coupling efficiency and quality factor," Opt. Express **18**, 16064–16073 (2010).
47. N. Vico Triviño, U. Dharanipathy, J.-F. Carlin, Z. Diao, R. Houdré, and N. Grandjean, "Integrated photonics on silicon with wide bandgap GaN semiconductor," Appl. Phys. Lett. **102**, 081120 (2013).
48. M. Galli, S. Portalupi, M. Belotti, L. Andreani, L. O'Faolain, and T. Krauss, "Light scattering and Fano resonances in high-*Q* photonic crystal nanocavities," Appl. Phys. Lett. **94**, 071101 (2009).
49. S.-H. Kim and Y.-H. Lee, "Symmetry relations of two-dimensional photonic crystal cavity modes," IEEE J. Quantum Electron. **39**, 1081–1085 (2003).
50. K. Hennessy, C. Högerle, E. Hu, A. Badolato, and A. Imamoğlu, "Tuning photonic nanocavities by atomic force microscope nano-oxidation," Appl. Phys. Lett. **89**, 041118 (2006).
51. R. Camacho-Morales, M. Rahmani, S. Kruk, L. Wang, L. Xu, D. A. Smirnova, A. S. Solntsev, A. Miroshnichenko, H. H. Tan, F. Karouta, S. Naureen, K. Vora, L. Carletti, C. De Angelis, C. Jagadish, Y. S. Kivshar, and D. N. Neshev, "Nonlinear generation of vector beams from AlGaAs nanoantennas," Nano Lett. **16**, 7191–7197 (2016).
52. Z. Lin, M. Lončar, and A. W. Rodriguez, "Topology optimization of multi-track ring resonators and 2d microcavities for nonlinear frequency conversion," Opt. Lett. **42**, 2818–2821 (2017).
53. K. Koshelev, S. Kruk, E. Melik-Gaykazyan, J.-H. Choi, A. Bogdanov, H.-G. Park, and Y. Kivshar, "Subwavelength dielectric resonators for nonlinear nanophotonics," Science **367**, 288–292 (2020).